

March 1, 2021

TO: Distribution

FROM: Shantanu P. Naidu, Steven R. Chesley, Davide Farnocchia
Solar System Dynamics Group (392R), Jet Propulsion Laboratory,
California Institute of Technology

SUBJECT: Computation of the orbit of the satellite of binary near-Earth asteroid (65803) Didymos.

We used the times of occultations and eclipses observed in lightcurves from 2003, 2015, 2017, and 2019 to estimate the orbit of the satellite of (65803) Didymos relative to Didymos. We used a weighted least-squares approach with square root information filtering for the estimation. The data is consistent with three separate solutions corresponding to different values of Binary YORP, a radiative effect that could cause a drift in mean motion. The three nominal solutions are separated by about 50° in orbital phase during the planned DART mission impact in October 2022 and their formal 3σ uncertainties are about 30° for each. Observations in January to March 2021 should eliminate at least one, probably two, of the three solutions. Additional observations in July 2022 should almost certainly allow the identification of the correct solution. Using synthetic observations in 2021 and 2022, we estimate that the formal 3σ uncertainty in the orbital phase during the DART impact will be $< 5^\circ$. These results are preliminary and subject to internal review.

1 Introduction

The Binary near-Earth asteroid (NEA) (65803) Didymos is the target of NASA's Double Asteroid Redirection Test (DART) mission (Cheng et al., 2016) and the European Space Agency's Hera mission (Michel et al., 2018). Didymos was discovered in 1996 by the Spacewatch telescope at Kitt Peak (MPEC 1996 H03) and its binary nature was discovered in 2003 by Pravec et al. (2003). The primary and secondary components are roughly 780 m and 150 m in diameter, respectively, and the mutual orbit of the system has a semimajor axis of ~ 1.2 km and a period of about 11.9 h (Pravec et al., 2006; Naidu et al., 2019).

The DART mission is a planetary defense experiment with a planned launch in July 2021. The mission consists of a spacecraft that would impact the satellite of Didymos in October 2022 and change its orbital period around Didymos by > 1 min. The change would be measured by ground-based photometric and radar observations over several months after the impact. The Hera mission will characterize Didymos and its satellite starting in 2026.

The requirements on the orbital phase uncertainties during different mission milestones are given in Table 1.

Table 1: Requirements on the 3σ uncertainty of the true anomaly of the satellite at different mission milestones.

Milestone	Approximate Date	Didymos B true anomaly 3σ uncertainty at DART encounter.
60 days prior to launch	23 May 2021	$\pm 45^\circ$
55 days prior to impact	03 Aug 2022	$\pm 15^\circ$

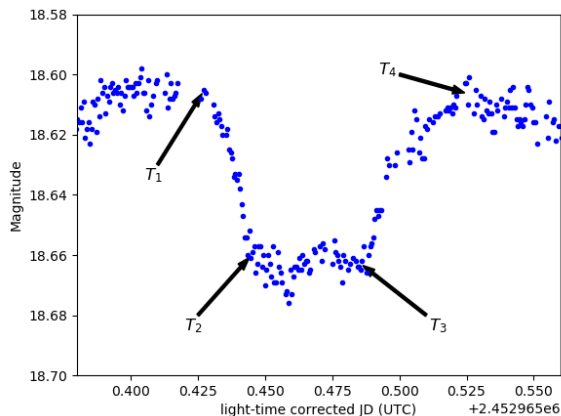


Figure 1: A secondary eclipse event showing the four contact times.

2 Observations

We used the times of mutual events (occultations and eclipses) detected in photometric observations of Didymos to determine the orbit of the satellite of Didymos with respect to the primary. The dataset includes observations from 2003 (Pravec et al., 2006), 2015, 2017, and 2019 (Pravec and Scheirich, personal communication). There are four different kinds of mutual events in the data: eclipse of the primary (secondary casting shadows on the primary), eclipse of the secondary, occultation of the primary from the point of view of the observer, and occultation of the secondary.

A mutual event causes a brief drop in the brightness of the system and typically has four contact times: the first contact is when the event begins and the brightness starts decreasing, the second contact is when the brightness reaches a minimum, the third contact is when the brightness starts increasing again, and the fourth contact is when the event ends. We use T_1 , T_2 , T_3 , and T_4 to refer to these contact times. Figure 1 shows contact times for a secondary eclipse event from 2003. We used the mid-times between T_1 and T_2 , and T_3 and T_4 as our observations. These would be the approximate start and end times of each event if the satellite was a point. These mid-contact times are referred as $T_{1.5}$ and $T_{3.5}$ in this memo. In some cases two events overlap: for example, if the phase angle (Sun-asteroid-observer angle) is low, an eclipse and an occultation can occur at the same time.

Pravec and Scheirich (personal communication) provided start and end times (T_1 and T_4) of the

events based on their full lightcurve modeling. We used these times as guidelines for identifying the events and contacts by plotting the lightcurves provided by Pravec and Scheirich. $T_{1.5}$ and $T_{3.5}$ were then measured as $(T_1 + T_2)/2$ and $(T_3 + T_4)/2$, respectively, and 1σ uncertainties of about $(T_2 - T_1)/4$ and $(T_4 - T_3)/4$ were assigned. In some cases, when the lightcurves were noisier than usual, larger uncertainties were assigned. The observations and their uncertainties are listed in Table 2. Observations represent the UTC times at which the light was emitted from the asteroid, and so are one-way light-time corrected with respect to the Earth.

3 Methods

3.1 Orbit fit

We used a weighted least-squares method to estimate the best-fit model parameters. The goal is to minimize the cost function, $\chi^2 = \nu^T W \nu$, where ν is the array of residuals (observed - modeled) and W is the weight matrix with $W_{i,j} = 0$ for $i \neq j$, and $W_{i,j} = 1/\sigma_i^2$ for $i = j$. Here σ_i is the observational uncertainty for the i th observation.

The least-squares solution is found by iteratively correcting the estimated parameters x by

$$\Delta x = -\Gamma B^T W \nu, \quad (1)$$

where $B = \partial \nu / \partial x$ is the design matrix, $\Gamma = C^{-1}$ is the covariance matrix, and $C = B^T W B$ is the normal matrix, also called the information matrix. This iterative procedure is called differential corrections. The marginal 1σ uncertainties of the parameters are computed by taking the squareroot of the diagonal elements of the covariance matrix.

We used the NAIF SPICE geometry finder tools (Acton et al., 2018) for modeling the times of the observed events. This requires creating SPICE kernels that describe the trajectory, size, shape, and orientation of the objects. We modeled the primary as an oblate spheroid with dimensions of 830 x 830 x 786 m (Naidu et al., 2019) with its spin pole aligned with the mutual orbit pole. This information is defined in a planetary constants kernel (PCK) file. The primary was treated as an ellipsoid for computing the mutual event timings but was treated as a point mass for modeling the mutual orbit.

We assumed the satellite to be a point mass on a modified Keplerian mutual orbit around the primary. In addition to Keplerian motion, we included an additional term for modeling the drift in mean motion due to Binary YORP (BYORP) (Ćuk, 2007). Since the system mass is constant, a drift in mean motion leads to a change in semimajor axis with time. The mean anomaly (M) and mean motion (n) of the satellite at time t are given by:

$$\begin{aligned} M(t) &= M_0 + n_0(t - t_o) + \frac{1}{2}\dot{n}(t - t_o)^2, \\ n(t) &= n_0 + \dot{n}(t - t_o), \end{aligned} \quad (2)$$

Table 2: Mutual event times measured in observations from 2003, 2015, 2017, and 2019. Contacts 1.5 and 3.5 indicate the mid-times between first and second contacts and between third and fourth contacts respectively.

LT corrected event time (JD UTC)	Contact	Occulted/Eclipsed object	Event type	1σ Uncertainty (days)
2003				
2452964.502	3.5	Secondary	Eclipse	0.005
2452965.435	1.5	Secondary	Eclipse	0.004
2452965.506	3.5	Secondary	Eclipse	0.010
2452965.696	1.5	Primary	Eclipse	0.075
2452965.747	3.5	Primary	Eclipse	0.006
2452966.682	1.5	Primary	Eclipse	0.007
2452966.729	3.5	Primary	Eclipse	0.006
2452967.681	1.5	Primary	Eclipse	0.009
2452967.727	3.5	Primary	Eclipse	0.005
2452969.653	1.5	Primary	Eclipse	0.007
2452969.705	3.5	Primary	Eclipse	0.008
2452971.393	1.5	Secondary	Eclipse	0.004
2452973.375	1.5	Secondary	Eclipse	0.005
2452973.625	1.5	Primary	Eclipse	0.004
2452975.664	3.5	Primary	Occultation	0.006
2452976.646	3.5	Primary	Occultation	0.008
2452976.849	1.5	Secondary	Eclipse	0.005
2452976.899	3.5	Secondary	Occultation	0.010
2452977.596	1.5	Primary	Eclipse	0.005
2452977.645	3.5	Primary	Occultation	0.005
2452990.749	1.5	Secondary	Eclipse	0.008
2452990.797	3.5	Secondary	Eclipse	0.005
2452992.286	3.5	Secondary	Occultation	0.005
2452992.483	1.5	Primary	Eclipse	0.008
2452992.526	3.5	Primary	Occultation	0.010
2452992.728	1.5	Secondary	Eclipse	0.005
2452992.780	3.5	Secondary	Occultation	0.008
2452993.719	1.5	Secondary	Eclipse	0.005
2452993.771	3.5	Secondary	Occultation	0.008
2015				
2457125.697	3.5	Primary	Occultation	0.010
2457126.894	1.5	Secondary	Eclipse	0.010
2017				
2457809.670	1.5	Primary	Occultation	0.010
2457809.722	3.5	Primary	Eclipse	0.008
2457843.456	1.5	Primary	Eclipse	0.008
2457843.488	3.5	Primary	Occultation	0.008
2457843.706	1.5	Secondary	Eclipse	0.008
2457843.739	3.5	Secondary	Occultation	0.005
2457861.824	1.5	Primary	Eclipse	0.005
2457870.760	1.5	Primary	Eclipse	0.005
2457877.768	3.5	Primary	Occultation	0.008
2019				
2458514.861	3.5	Secondary	Eclipse	0.005
2458515.041	1.5	Primary	Occultation	0.006

Here M_0 and n_0 are mean anomaly and mean motion of the satellite at time t_0 , and \dot{n} is the constant rate of change of mean motion due to BYORP. These equations were used to generate the states of the satellite with respect to the primary at 1-day intervals and the corresponding SPK files. We used type-5 SPKs, which assume Keplerian motion for interpolating states. The time interval between states is small enough that errors in mean motion due to BYORP are orders of magnitude smaller than the uncertainty. Tests with 0.001 day intervals yield almost identical results.

Once the required SPICE kernels were written, mutual event times were computed using the ‘gfo-
clt’ module in SPICE. The output of ‘gfo-
clt’ are times when the photons are emitted from the Sun (for eclipses) or times when the photons reach Earth (for occultations) however the observations listed in Table 2 are times when the observed photons were at the asteroid. In order to compute the residuals, appropriate one-way light-time corrections have to be made.

For eclipses, we estimated time intervals when the light emitted from the Sun underwent a primary or secondary eclipse event at the target. The ‘XLT’ (transmission case) aberration correction was used to obtain the target states when the light emitted from the Sun reached the target. One-way light-times between the Sun and the asteroid were then computed using the SPICE routine ‘ltime’ and added to the output times to obtain the corresponding event times at the asteroid. All the calculations were performed in Barycentric Dynamical Time (TDB) and the results were later converted to UTC.

For occultations, we estimated time intervals when the satellite was occulted by or in transit across the primary as seen from Earth. The ‘LT’ aberration correction was used to obtain the target states when the light received at Earth was emitted from the target. One-way light-times between the asteroid and the Earth were then computed using the SPICE routine ‘ltime’ and subtracted from the output times to obtain the corresponding event times at the asteroid.

The design matrix, $\partial\nu/\partial x$, was computed numerically using second order central differences:

$$\left. \frac{\partial\nu}{\partial P} \right|_{P_i} = \frac{-\nu(P_i + 2\delta P) + 8\nu(P_i + \delta P) - 8\nu(P_i - \delta P) + \nu(P_i - 2\delta P)}{12\delta P}, \quad (3)$$

where δP is a small increment in the value of the parameter. The values for δP were carefully chosen by numerically testing the values of the partials. For M_0 , n_0 , and \dot{n} the increments were 0.01 rad, 10^{-10} rad s⁻¹, and 5×10^{-18} rad s⁻².

We used the following estimates from Pravec et al. (2006), Scheirich and Pravec (2009), and Naidu et al. (2019) as our initial conditions: semimajor axis = 1.2 km, eccentricity = 0, longitude of ascending node = 40°, inclination = 174°, and orbital period = 11.9216 h. All angles are in the SPICE ECLIPJ2000 reference frame. Since eccentricity = 0, the mean anomaly is measured from the ascending node. We started by estimating M_0 , n_0 , and \dot{n} using data from 2003. We then incrementally added data from 2015, 2017, and 2019 to obtain tighter constraints on the solution.

3.2 Predictions

The nominal values of M , n , and \dot{n} are propagated to a time t using equations 2. The covariance matrix is mapped to a different epoch using:

$$\Gamma_t = S\Gamma_0S^T \quad (4)$$

where

$$S = \frac{\partial(M_t, n_t, \dot{n}_t)}{\partial(M_0, n_0, \dot{n}_0)} = \begin{bmatrix} \frac{\partial M_t}{\partial M_0} & \frac{\partial M_t}{\partial n_0} & \frac{\partial M_t}{\partial \dot{n}_0} \\ \frac{\partial n_t}{\partial M_0} & \frac{\partial n_t}{\partial n_0} & \frac{\partial n_t}{\partial \dot{n}_0} \\ \frac{\partial \dot{n}_t}{\partial M_0} & \frac{\partial \dot{n}_t}{\partial n_0} & \frac{\partial \dot{n}_t}{\partial \dot{n}_0} \end{bmatrix} = \begin{bmatrix} 1 & (t - t_0) & \frac{1}{2}(t - t_0)^2 \\ 0 & 1 & (t - t_0) \\ 0 & 0 & 1 \end{bmatrix}$$

Here subscripts t and 0 denote parameters at time t and t_0 respectively. The marginal 1σ uncertainties on the parameters are the square roots of the corresponding diagonal elements of Γ_t . The uncertainty on \dot{n} does not change with time.

Similarly, predictions of observable uncertainties at time t are computed as:

$$\Gamma_{T_*} = Q\Gamma_tQ^T, \quad (5)$$

where

$$Q = \frac{\partial T_*}{\partial(M_t, n_t, \dot{n})}. \quad (6)$$

Here Q is computed numerically using second order central differences and T_* is the observed event time.

4 Results

Table 3 shows the best-fit solution to the 2003 data. The formal 3σ uncertainty in mean anomaly, when mapped to the 2015 apparition, is close to about 2000 revolutions of the satellite around the primary. The large uncertainty allows several distinct solutions, corresponding to different numbers of complete orbits, to be consistent with the 2003 and 2015 data. We found about 30 local minima in χ^2 by fitting the data from the two apparitions starting with several trial values of n spaced 10^{-9} rad s $^{-1}$ apart within the 3σ uncertainty region of the 2003 solution. Of these, the three solutions listed in Table 4 fit the entire dataset from 2003-2019. Table 5 shows the full covariance of solution 1. Covariances corresponding to solutions 2 and 3 are not materially different. Table 6 provides the corresponding covariance when mapped to the epoch of the DART encounter.

The three solutions in Table 4 differ in the direction and magnitude of the BYORP term \dot{n} : solution 1 is consistent with no significant BYORP, solutions 2 and 3 have a positive and a negative value of \dot{n} , respectively. These values of \dot{n} are in family with those estimated for binary asteroids (66391) 1999 KW4 and (88710) 2002 SL9 (Scheirich et al., 2019). In terms of the χ^2 values, solution 1 provides the best fit and therefore appears the most likely. Solution 2 has only a modestly higher value of χ^2 and is therefore somewhat less likely, but not markedly so. Solution 3 has a

Table 3: Best-fit orbital parameters to the 2003 data. M_0 , n_0 and \dot{n} were fit. Pole (λ, β) is not estimated and is from Pravec and Scheirich (personal communication). Period is derived from n_0 . $\chi^2_\nu = \chi^2/(n_{obs} - n_{est})$ is the reduced χ^2 , where n_{obs} is the number of observations and n_{est} is the number of estimated parameters.

Parameter	Value	1σ uncertainty
M_0 ($^\circ$)	355.2	2.1
Period (h)	11.9195	0.0058
n_0 (rad s $^{-1}$)	1.46426e-04	0.00071e-4
\dot{n} (rad s $^{-2}$)	-2.7e-14	4.9e-14
Epoch (TDB)	2003-11-20.0	
χ^2	16.4	
χ^2_ν	0.63	
$(\lambda, \beta)^\circ$	(310, -84) $^\circ$	

Table 4: Best-fit orbital parameters to the entire dataset from 2003-2019. Only M_0 , n_0 and \dot{n} were fit. Pole (λ, β) is not estimated and is from Pravec and Scheirich (personal communication). Period is derived from n_0 . The best-fit parameters are similar to those reported by Scheirich and Pravec (personal communication)

Parameter	Value $\pm 1\sigma$		
	Solution 1	Solution 2	Solution 3
M_0 ($^\circ$)	355.31 ± 0.79	357.24 ± 0.79	353.39 ± 0.79
Period (h)	11.92170 ± 0.00006	11.92408 ± 0.00006	11.91933 ± 0.00006
n_0 (rad s $^{-1}$)	$(1.463994 \pm 0.000008) \times 10^{-4}$	$(1.463702 \pm 0.000008) \times 10^{-4}$	$(1.464285 \pm 0.000008) \times 10^{-4}$
\dot{n} (rad s $^{-2}$)	$(3.9 \pm 3.5) \times 10^{-18}$	$(7.1 \pm 0.4) \times 10^{-17}$	$(-6.3 \pm 0.4) \times 10^{-17}$
Epoch (TDB)	2003-11-20.0	2003-11-20.0	2003-11-20.0
χ^2	37.9	42.37	49.6
χ^2_ν	0.97	1.09	1.27
$(\lambda, \beta)^\circ$	(310, -84) $^\circ$	(310, -84) $^\circ$	(310, -84) $^\circ$

somewhat larger χ^2 and therefore seems to be the least likely of the three options. However we cannot conclusively rule out solutions 2 and 3 at present. Figure 2 shows the residuals of the three solutions.

As we added data from successive apparitions to generate new solutions we tested the ability of each solution to reliably predict observations not yet included in the fit. Figure 3 shows results from some of these tests using data from 2003 and 2015 to predict observations from 2017 and 2019 and data from 2003, 2015, and 2017 to predict observations in 2019. All predictions from the 2003-2015 fits are $< 1.5\sigma$ from the observed values. Fits corresponding to solution 1 consistently generated predictions within 1σ of the observed values. Fits to the 2003-2015 data corresponding to solutions 2 and 3 generate satisfactory predictions for the 2017 and 2019 data but after including the 2017 data, predictions to one of the observations in 2019 are about 2.5σ off.

Figure 4 shows the projections of these solution parameters and their covariances. In this figure and elsewhere in this memo, orbital phase is the angle in the orbital plane measured from the 0° longitude in the ECLIPJ2000 frame, as opposed to mean anomaly, which is measured from the ascending node. Both angles are measured in the direction of the orbital motion of the satellite.

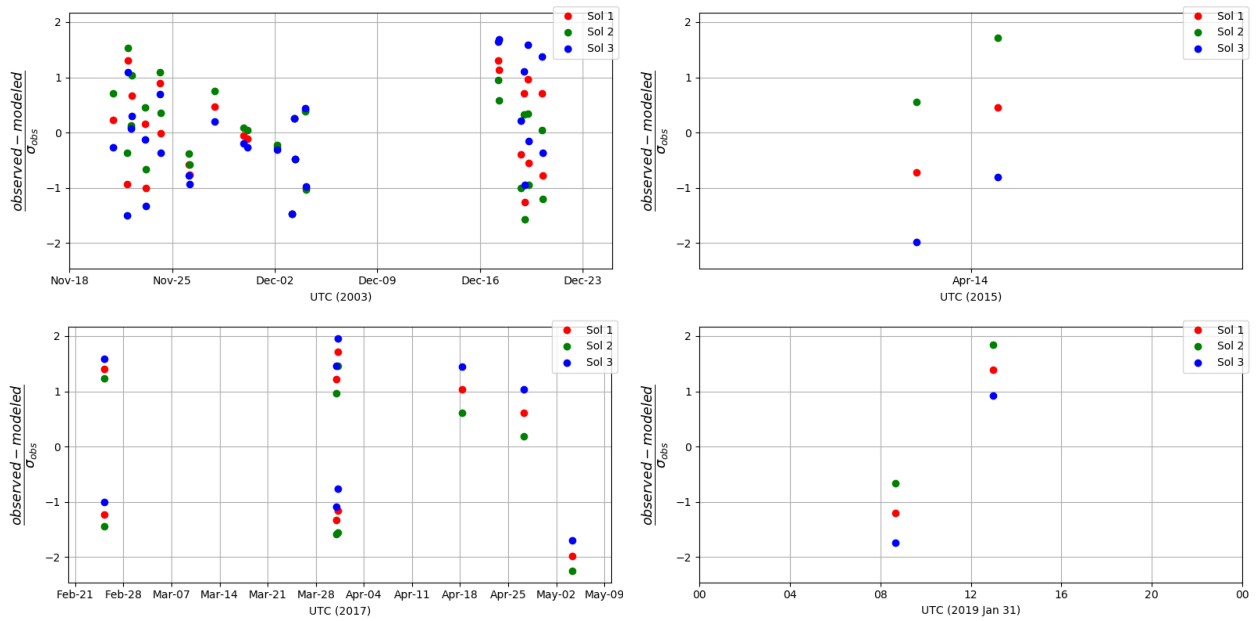


Figure 2: Residuals (observed-modeled) of the three solution from Table 4. Each panel shows residuals from a different apparition. Red, green, and blue colors show residuals from solutions 1, 2, and 3, respectively.

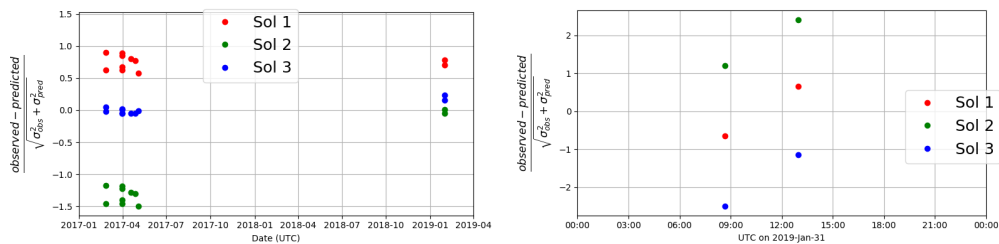


Figure 3: The left panel shows the comparison between predictions generated using observations from 2003 and 2015 to observations in 2017 and 2019. The right panel shows predictions generated using 2003, 2015, and 2017 data. The red, green, and blue points show predictions from solutions corresponding to solutions 1, 2, and 3, respectively, from Table 4 but using only partial datasets.

Table 5: Covariance matrix corresponding to solution 1 at 2003-Nov-20.0 TDB. Covariances for solutions 2 and 3 are not materially different. Units of the parameters are in radians and seconds.

	M_0	n_0	\dot{n}
M_0	1.92017685e-04	-1.57090318e-12	5.16374265e-21
n_0	-1.57090318e-12	5.97244064e-19	-2.71272824e-27
\dot{n}	5.16374265e-21	-2.71272824e-27	1.24028419e-35

Table 6: Covariance matrix from Table 5 mapped to 2022-Oct-01.0 TDB, the epoch of the DART impact.

	M_0	n_0	\dot{n}
M_0	2.89232683e-02	2.23294056e-10	5.87930456e-19
n_0	2.23294056e-10	1.76277749e-18	4.67063393e-27
\dot{n}	5.87930456e-19	4.67063393e-27	1.24028419e-35

We performed similar fits starting with data from the final apparitions (2017-2019) and incrementally adding data from earlier apparitions. Figure 5 shows the projected solutions from these fits. As additional data is included in the fit, the solutions stay within the 3σ confidence interval of the previous solutions, which lends confidence to the prediction generated by the solutions.

5 Future Observations

There are two future observing opportunities before the planned DART impact date. One from January to March 2021 and another beginning around June 2022 and continuing through the DART impact. We performed a covariance analysis to quantify the effects of observations during these observing windows on the solution uncertainties.

Figure 6 shows the orbital phases predicted by the three solutions from Table 4 during the 2021 observing window. The three solutions are separated from each other by approximately their 3σ uncertainties of $\sim 18^\circ$. We generated three sets of synthetic observations between January and March, 2021 corresponding to each of the three solutions and measured the effects of each set on the χ^2 values of each solution. Table 7 shows the results. If observations in 2021 fall close to the nominal predictions of solution 1 (row 1 of Table 7), then it should be possible to rule out solutions 2 and 3 due to higher χ^2 values. If the observations fall close to the nominal predictions of solutions 2 or 3 (rows 2 and 3), then one of the solutions can be ruled out based on its significantly higher χ^2 value. We performed similar tests by adding synthetic observations between January and March 2021 and between June and September 2022 (Table 8). The effects of the additional observations from 2022 on the χ^2 values are more pronounced suggesting that they will probably identify the correct solution.

Figure 7 shows the orbital phases at the time of the DART encounter predicted by solutions 1, 2, and 3. The three solutions are separated by about 50° from each other and have 3σ uncertainties of about 30° each with the current data set. However, future observations should reduce these

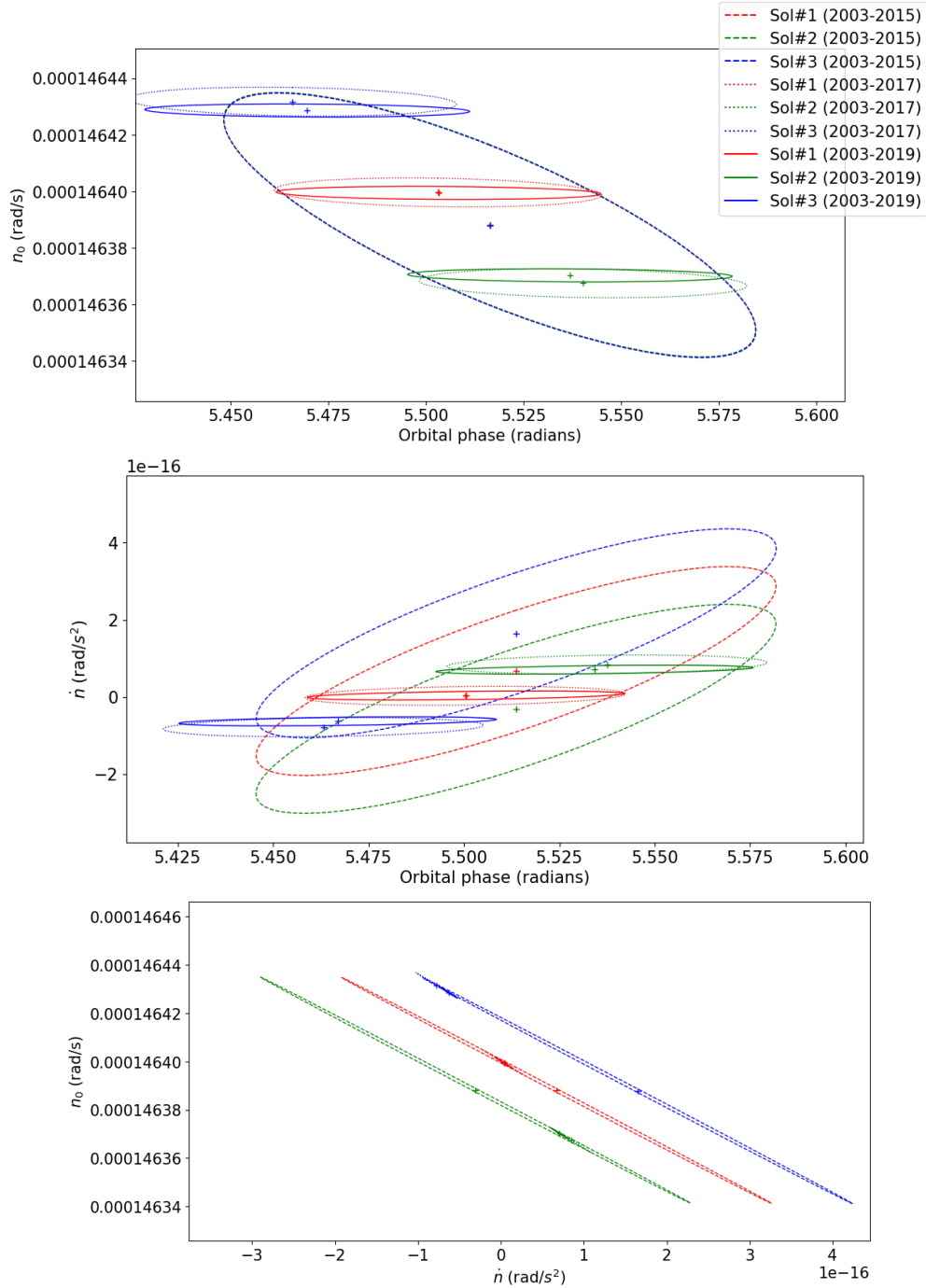


Figure 4: Projections of the best-fit parameters and their 3σ uncertainty regions from the forward prediction tests. Red, Green, and blue lines show fits corresponding solutions 1, 2, and 3 in Table 4. Dashed, dotted, and solid lines lines show fits to data from 2003-2015, 2003-2017, and 2003-2019 respectively. The last are the solutions listed in Table 4. Fits to only the 2003 data (not shown) encompass fits with more data. Solutions are at epoch 2003-11-20.0 TDB.

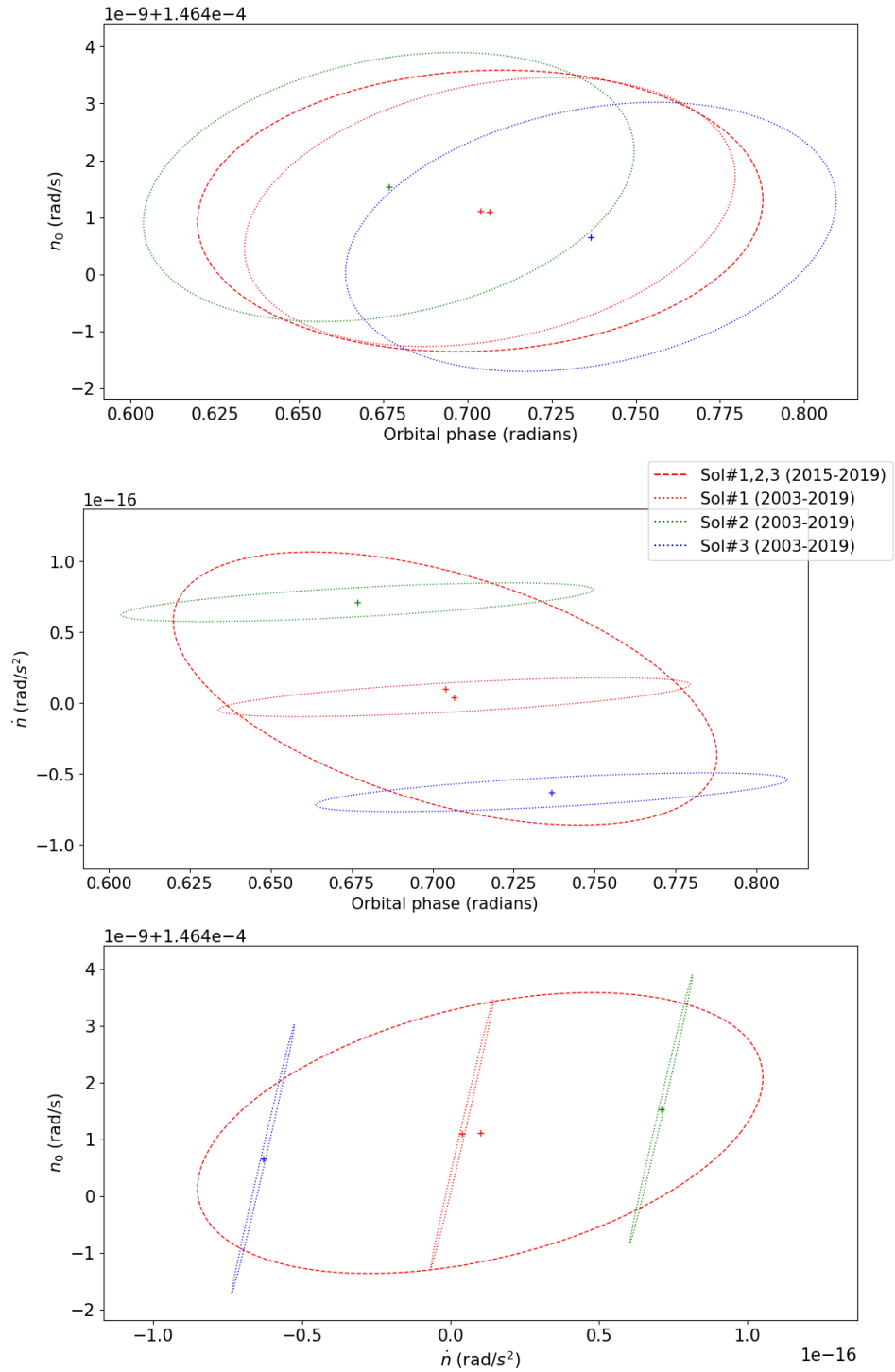


Figure 5: Projections of the best-fit parameters and their 3σ uncertainty regions from the backward prediction tests. Red dashed curve shows the solution using the 2015-2019 data. Red, Green, and blue dotted lines show fits corresponding to solutions 1, 2, and 3 in Table 4 using data from 2003-2019. Fits to 2017-2019 data (not shown) encompass fits with more data. Solutions are at epoch 2017-Nov-20.0 TDB.

Table 7: χ^2 values of the three solutions after adding synthetic observations in 2021 generated using the three solutions. Synthetic obs. 1, 2, and 3 are generated from solutions 1, 2, and 3, respectively.

	Solution 1	Solution 2	Solution 3
Synthetic obs. 1	37.9	53.6	60.8
Synthetic obs. 2	49.1	42.4	94.6
synthetic obs. 3	49.1	87.2	49.6

Table 8: χ^2 values of the three solutions after adding synthetic 2021 and 2022 observations generated using the three solutions. Synthetic obs. 1, 2, and 3 are generated from solutions 1, 2, and 3, respectively.

	Solution 1	Solution 2	Solution 3
Synthetic obs. 1	37.9	97.8	105.0
Synthetic obs. 2	94.4	42.4	275.5
synthetic obs. 3	93.3	264.2	49.6

uncertainties as shown in Figure 8. The potential 3σ orbital phase uncertainties during the DART encounter assuming observations in 2021, and observations in 2021 and 2022, are about 6° and 3° , respectively.

If observations in 2021 identify the correct solution, then the 3σ orbital phase uncertainty of 6° on that solution will already satisfy the mission requirement for 55 days before impact (Table 1, row 2). However, if there are two solutions remaining after 2021 our simulations indicate that the orbital phase separation at encounter will be reduced from 50° to 15° , which would allow the pre-launch mission requirement to be satisfied (Table 1, row 1). But in that case additional observations in 2022 would be required to meet the pre-impact requirement (Table 1, row 2).

6 Sensitivity to unestimated parameters

The uncertainties of the solutions in Table 4 and the covariances in Tables 5 and 6 do not take into account variations due to the size of the primary, orbit pole, eccentricity, argument of pericenter, and the obliquity of the orbit pole with respect to the spin pole of the primary. We conducted sensitivity tests for these parameters to quantify their contributions to the uncertainties. In these tests we varied the unestimated parameters within their assumed 3σ uncertainty regions, computed a corresponding least-squares solution for M_0 , n_0 , and \dot{n} , and measured the change in orbital phase at the time of the DART encounter. Figure 9 shows the results from one such test with respect to the orbit pole. Based on these tests we recommend that the formal uncertainties derived from the covariance matrices in Tables 5 and 6 should be scaled up by a factor of 1.3 in order to capture the possible systematic errors due to the unestimated parameters.

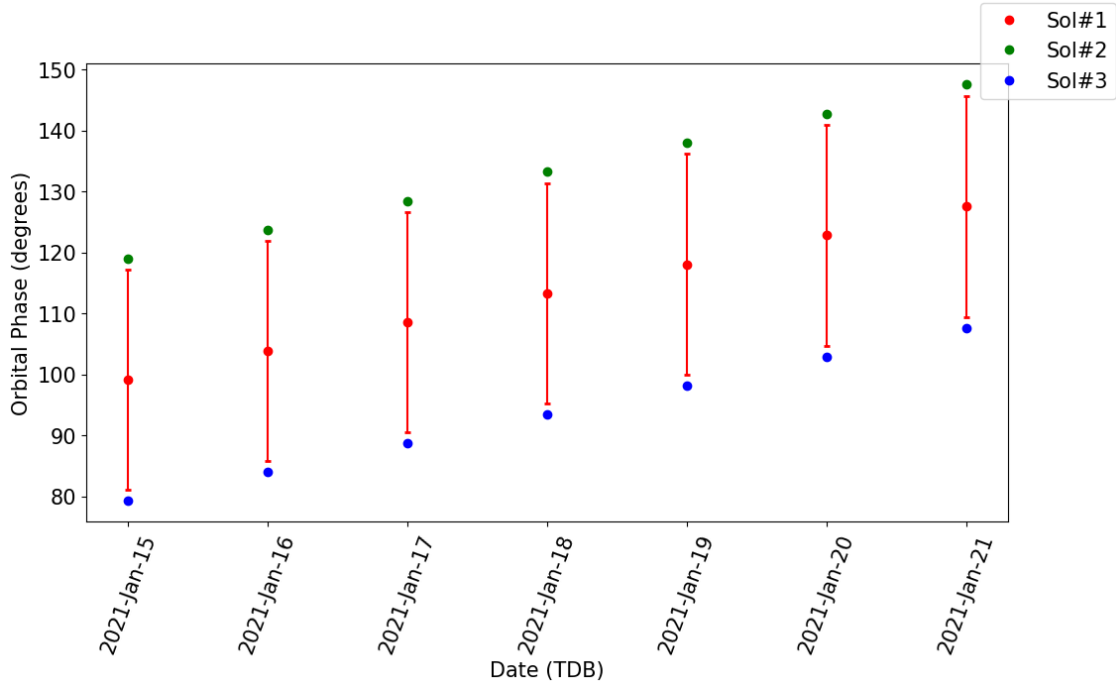


Figure 6: Orbital phases and 3σ uncertainties predicted by the three solutions from Table 4 at the beginning of the next observing opportunity in January 2021. All solutions have the same 3σ uncertainties of $\sim 18^\circ$ (only shown for solution 1) and are separated by about 3σ .

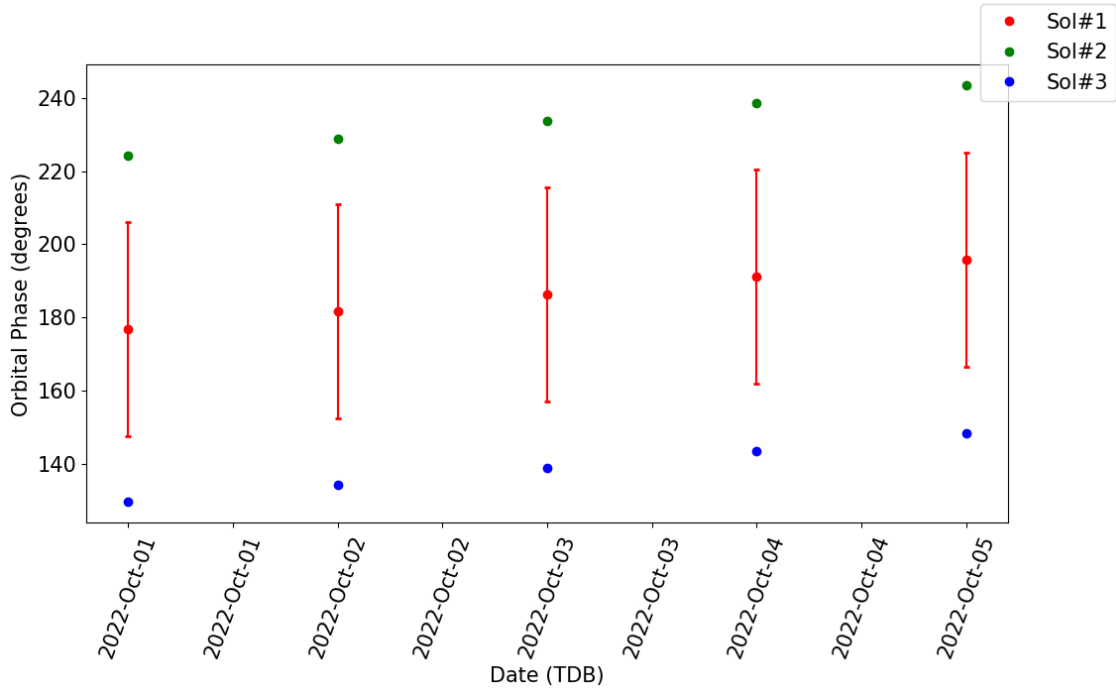


Figure 7: Orbital phases and 3σ uncertainties predicted by the three solutions from Table 4 during the DART encounter in October 2022. All solutions have the same 3σ uncertainties of about 30° (only shown for solution 1).

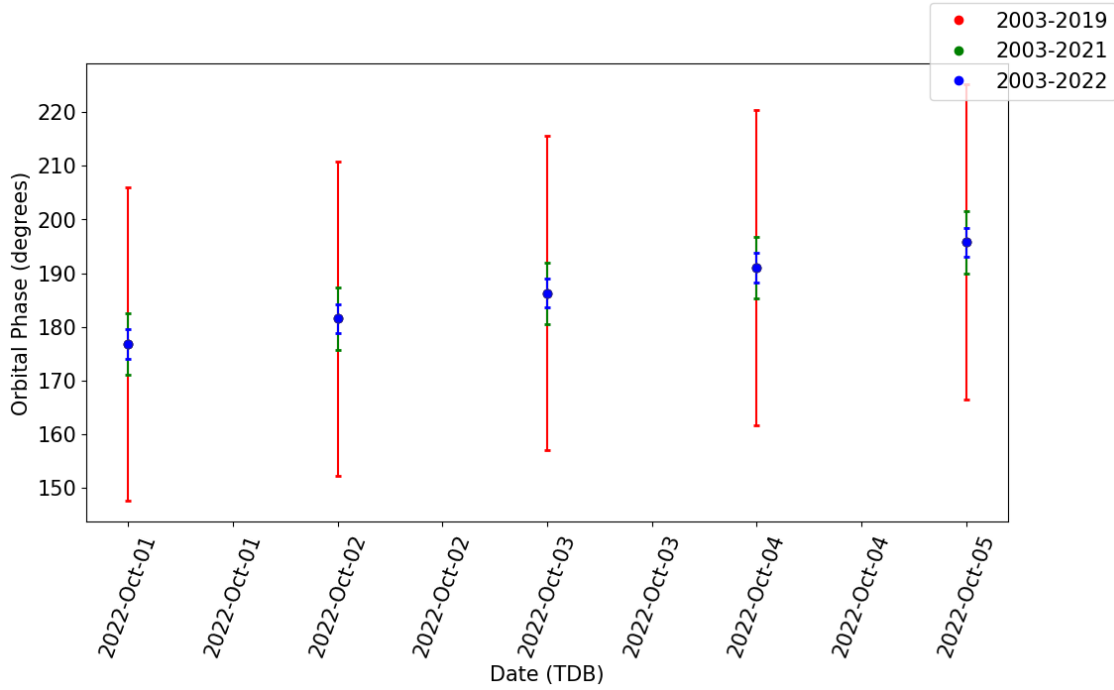


Figure 8: Predicted 3σ orbital phase uncertainties for the solution 1 during the planned DART encounter assuming no additional observations beyond 2019 (red), observations in 2021 (green), and observations in 2021 and 2022 (blue). The 3σ uncertainties for the three cases are about 30° , 6° , and 3° respectively. Solutions 2 and 3 (not shown) have similar uncertainties.

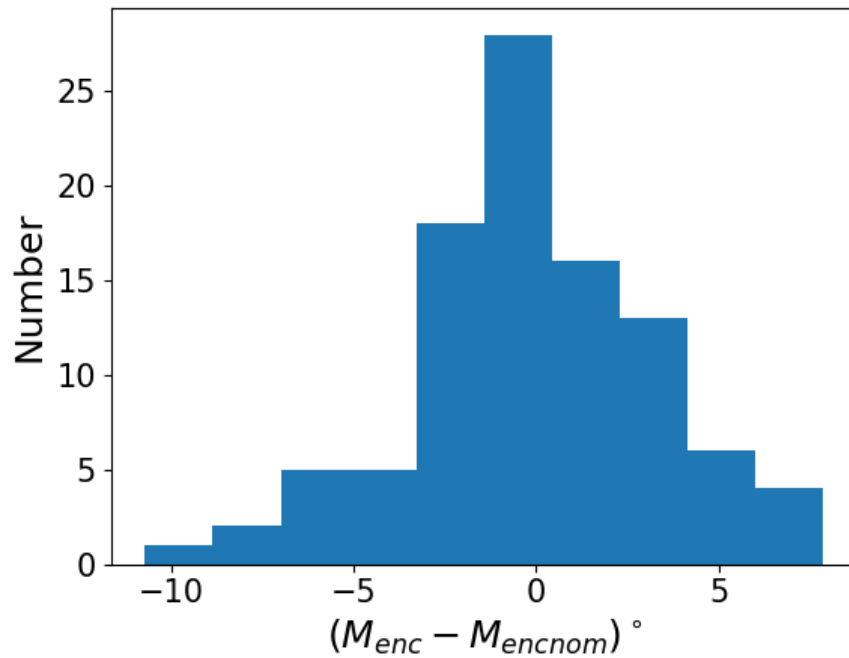


Figure 9: Histogram of the change in orbital phase at the time of the DART encounter due to variations in orbit pole within 10° of the nominal. This test was conducted with 100 test cases.

7 Conclusion

We deliver SPK files named ‘solution1.bsp’, ‘solution2.bsp’, and ‘solution3.bsp’, corresponding to solutions 1, 2, and 3 from Table 4, respectively, as the best-fit orbits to the available mutual event data obtained between 2003 and 2019. Tables 5 and 6 list the corresponding covariance matrices at epochs 2003-Nov-20.0 TDB and 2022-Oct-01.0 TDB, respectively. We suggest scaling the formal uncertainties derived from these covariances by a factor of 1.3 in order to capture contributions from unmodeled parameters. Future observations in 2021 and 2022 should be able to identify the correct solution. If observations in 2021 identify the correct solution, the mission requirement at 55 days prior to impact (Table 1) would be met without any additional data. Data from 2022 will likely allow those requirements to be met.

Acknowledgement

This work was carried out at the Jet Propulsion Laboratory, California Institute of Technology, under a contract with the National Aeronautics and Space Administration (80NM0018D0004).

References

- Acton, C., Bachman, N., Semenov, B., and Wright, E. (2018). A look towards the future in the handling of space science mission geometry. *Planetary and Space Science*, 150:9–12.
- Cheng, A. F., Michel, P., Jutzi, M., Rivkin, A. S., Stickle, A., Barnouin, O., Ernst, C., Atchison, J., Pravec, P., Richardson, D. C., and AIDA Team (2016). Asteroid Impact & Deflection Assessment mission: Kinetic impactor. *planss*, 121:27–35.
- Ćuk, M. (2007). Formation and Destruction of Small Binary Asteroids. *ApJL*, 659(1):L57–L60.
- Michel, P., Kueppers, M., Sierks, H., Carnelli, I., Cheng, A. F., Mellab, K., Granvik, M., Kestilä, A., Kohout, T., Muinonen, K., et al. (2018). European component of the aida mission to a binary asteroid: Characterization and interpretation of the impact of the dart mission. *Advances in Space Research*, 62(8):2261–2272.
- Naidu, S., Benner, L. A. M., Brozovic, M., Nolan, M. C., Ostro, S. J., Margot, J. L., Giorgini, J. D., Hirabayashi, T., Scheeres, D. J., Pravec, P., Scheirich, P., Magri, C., and Jao, J. S. (2019). Radar observations and a physical model of binary near-Earth asteroid 65803 Didymos, target of the DART mission. *Icarus*.
- Pravec, P., Benner, L. A. M., Nolan, M. C., Kusnirak, P., Pray, D., Giorgini, J. D., Jurgens, R. F., Ostro, S. J., Margot, J. L., Magri, C., Grauer, A., and Larson, S. (2003). (65803) 1996 GT. *IAUCIRC*, 8244:2.
- Pravec, P., Scheirich, P., Kušnirák, P., Šarounová, L., Mottola, S., Hahn, G., Brown, P., Esquerdo, G., Kaiser, N., Krzeminski, Z., Pray, D. P., Warner, B. D., Harris, A. W., Nolan, M. C., Howell, E. S., Benner, L. A. M., Margot, J. L., Galád, A., Holliday, W., Hicks, M. D., Krugly, Y. N., Tholen, D., Whiteley, R., Marchis, F., DeGraff, D. R., Grauer, A., Larson, S., Velichko, F. P., Cooney, W. R., Stephens, R., Zhu, J., Kirsch, K., Dyvig, R., Snyder, L., Reddy, V., Moore, S., Gajdoš, Š., Világi, J., Masi, G., Higgins, D., Funkhouser, G., Knight, B., Slivan, S., Behrend, R., Grenon, M., Burki, G., Roy, R., Demeautis, C., Matter, D., Waelchli, N., Revaz, Y., Klotz, A., Rieugné, M., Thierry, P., Cotrez, V., Brunetto, L., and Kober, G. (2006). Photometric survey of binary near-Earth asteroids. *Icarus*, 181(1):63–93.
- Scheirich, P. and Pravec, P. (2009). Modeling of lightcurves of binary asteroids. *Icarus*, 200(2):531–547.
- Scheirich, P., Pravec, P., Kušnirák, P., Hornoch, K., McMahon, J., Scheeres, D. J., Čapek, D., Pray, D. P., Kučáková, H., Galád, A., Vraštil, J., Krugly, Y. N., Moskovitz, N., Avner, L. D., Skiff, B., McMillan, R. S., Larsen, J. A., Brucker, M. J., Tubbiolo, A. F., Cooney, W. R., Gross, J., Terrell, D., Burkhonov, O., Ergashev, K. E., Ehgamberdiev, S. A., Fatka, P., Durkee, R., Lilly Schunova, E., Inasaridze, R. Y., Ayvazian, V. R., Kapanadze, G., Gaftonyuk, N. M., Sanchez, J. A., Reddy, V., McGraw, L., Kelley, M. S., and Molotov, I. E. (2019). A satellite orbit drift in binary near-Earth asteroids (66391) 1999 KW4 and (88710) 2001 SL9 – Indication of the BYORP effect. *arXiv e-prints*, page arXiv:1912.06456.